BNL-212343-2019-JAAM

Transition Metal Substitution of Hollandite alpha-MnO2: Enhanced Potential and Structural Stability on Lithiation from First-Principles Calculation

A. B. Brady, P. Liu

To be published in "JOURNAL OF PHYSICAL CHEMISTRY C"

October 2019

Chemistry Department

Brookhaven National Laboratory

U.S. Department of Energy

USDOE Office of Science (SC), Basic Energy Sciences (BES) (SC-22)

Notice: This manuscript has been authored by employees of Brookhaven Science Associates, LLC under Contract No. DE-SC0012704 with the U.S. Department of Energy. The publisher by accepting the manuscript for publication acknowledges that the United States Government retains a non-exclusive, paid-up, irrevocable, world-wide license to publish or reproduce the published form of this manuscript, or allow others to do so, for United States Government purposes.

DISCLAIMER

This report was prepared as an account of work sponsored by an agency of the United States Government. Neither the United States Government nor any agency thereof, nor any of their employees, nor any of their contractors, subcontractors, or their employees, makes any warranty, express or implied, or assumes any legal liability or responsibility for the accuracy, completeness, or any third party's use or the results of such use of any information, apparatus, product, or process disclosed, or represents that its use would not infringe privately owned rights. Reference herein to any specific commercial product, process, or service by trade name, trademark, manufacturer, or otherwise, does not necessarily constitute or imply its endorsement, recommendation, or favoring by the United States Government or any agency thereof or its contractors or subcontractors. The views and opinions of authors expressed herein do not necessarily state or reflect those of the United States Government or any agency thereof.

Transition Metal Substitution of Hollandite α-MnO_2: Enhanced Potential and Structural Stability on Lithiation from First Principles Calculation

Alexander B. Brady,[†] Killian R. Tallman,[‡] Esther S. Takeuchi,[†,‡,§] Amy C. Marschilok,[†,‡,§]

Kenneth J. Takeuchi,[,†,‡] and Ping Liu*[,//]*

[†]*Department of Materials Science and Chemical Engineering and* [‡]*Department of Chemistry, State University of New York at Stony Brook, Stony Brook, New York 11794, United States*

[§]*Energy and Photon Sciences Directorate, Interdisciplinary Sciences Building, Building 734, and* [//]*Chemistry Department, Building 555, Brookhaven National Laboratory, Upton, New York 11973, United States*

Abstract

Hollandite α-MnO_2, consisting of manganese-oxygen octahedra, has recently attracted attention due to its high theoretical capacity, yet it suffers capacity degradation during repeated (de)lithiation. Here we use a new conceptual approach to substitute one of the Mn in the tunnel wall via the form of $Mn_{0.875}M_{0.125}O_2$ (M = Ti, V, Cr, Nb, Ru), aiming to increase the lithiation potential and attain the theoretical capacity via the enhanced structural stability, with the ultimate goal of improved capacity retention upon repeated (de)lithiation. A bottom-up screening using Density Functional Theory (DFT) was performed to identify the effect of the transition metal substitution on lithiation of α-MnO_2. The calculations reveal that substitution with electron accepting Cr ions results in a more significant increase in the lithiation potential of MnO_2 than the other substituents. In terms of structural stability, both Cr and Nb are capable of effectively stabilizing the tunnel structure of α-MnO_2 under increased levels of lithiation and thus, providing the opportunity for significant increases in the cyclability and delivered capacity. Our study not only discovers the new lithiation pathway and intermediates at the atomic level, but also develops the key concepts to optimize the lithiation potential and structural durability for future α-MnO_2-based materials. This approach opens a new avenue for materials design of 1D tunnel structured materials for use as stable host frameworks for electrochemical ion (de)insertion.

1. Introduction

The application of manganese oxide (MnO_x)-based materials in lithium batteries (LB) has attracted considerable attention.[1-4] Mn is environmentally friendly, capable of accommodating 3+ and 4+ oxidation states and is thus of interest as a material class.[5, 6] Manganese oxide based materials have a rich structural diversity.[7] When considering ion insertion materials, a common structural form is layered motif providing ion diffusion in two dimensions.[7, 8] However, lattice expansion and contraction associated with ion movement and electron transfer can also be accompanied by structural degradation and amorphization with loss of functional capacity. In contrast, the tunneled structures with a more rigid framework can often accommodate the presence of multiple cations.

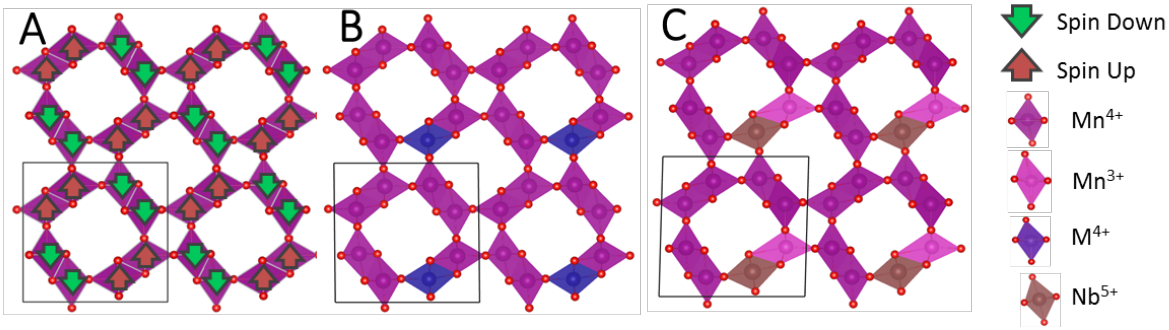

Figure 1. Structures of α-MnO_2(A), $Mn_{0.875}M_{0.125}O_2$(M= Ti, Cr, V, Ru) (B) and $Mn_{0.875}Nb_{0.125}O_2$ (C) (Red: O). The rectangle highlights the supercell considered in the calculation.

Hollandite (α-MnO_2) is a tunneled structure type which has been previously explored for battery, catalysis and capacitor applications.[4-6, 9, 10] α-MnO_2 has a one-dimensional 2 × 2 tunneled structure with the tunnel walls composed of edge-sharing MnO_6 octahedra. At the tunnel corners the MnO_6 octahedra meet in a corner-sharing arrangement surrounding a smaller 1 × 1 tunnel (Figure 1A). The open one-dimensional tunneled structure is known to contribute to facile diffusion with reduced polarization.[11] Its high voltage (3 Volts vs. Li/Li^+) and theoretical capacity (~300 mAh/g) make it an attractive candidate material for electrochemical energy storage.

A significant challenge for α-MnO_2 as a battery material is capacity retention upon repeated high levels of (de)lithiation.[12] Using *in-situ* synchrotron-based X-ray diffraction (XRD) and density functional theory (DFT),[13, 14] the Mn^{4+} (d^3) → Mn^{3+} (d^4) reduction upon lithiation was found to cause significant Jahn-Teller distortion and strain. The strain-induced asynchronous expansion of the unit cell resulted in symmetry degradation of α-MnO_2 as observed by *in-situ* transmission electron microscopy (TEM).[15] At a bulk level in active energy storage systems, evidence of Jahn-Teller distortion, partial irreversible dissolution of Mn^{3+} ions, and further destabilization of the structure upon cycling has been observed.[6,16]

A previously employed strategy to modify function of α-MnO_2 has been to add or modify a central cation including K^+, Ag^+, H^+, NH_4^+, or Ba^{2+} in the tunnels as part of the synthesis method.[4, 5, 14, 17, 18-20] The roles of K^+ and Ag^+ as the central cations have been investigated both experimentally[5, 20-23] and theoretically.[4, 24] Interestingly, while the compositional ranges show

some overlap, the compositional range for silver hollandite is typically >1.0 Ag per 8 Mn while that for potassium cryptomelane is more limited (typically <1.0 K per 8 Mn).[5] In contrast to this strategy, little attention has been paid to the possible effects of strategic replacement of Mn with another transition metal. Various transition metal substituents in MnO_2 motifs have been synthesized[6, 25-29] and studied to promote the catalytic activity of MnO_2.[30] Those studies show that substitution for transition metals in the MnO_2 structure can strongly affect both the electronic band structure and the crystal structure of MnO_2. The electrochemical impacts of such compositions have not yet been studied in lithium ion batteries.

Here for the first time DFT calculations were performed to identify the effect of substitution (M) on the stability and lithiation of α-MnO_2 via the composition of $Mn_{0.875}M_{0.125}O_2$. The substituents included both 3d (M = Ti, V, Cr) and 4d (M = Nb, Ru) metal ions. In terms of electronic modification, these ions can act as chemically inert (e.g. Ti^{4+}), electron donator (e.g. V^{4+}, Nb^{4+}), electron acceptor (e.g. Cr^{4+}), or a metallic (e.g. Ru^{4+}) substituent species in the substituted α-MnO_2 framework. In terms of atomic modification, the size difference between the substituted $M^{\delta+}$ ions and $Mn^{3+/4+}$ ions can cause the additional distortion in the tunnel structure of α-MnO_2. The present study first provides mechanistic understanding at the atomic level, enabling the discovery of a new lithiation pathway via the semi-layered transition. In addition, it pinpoints how such diversity in the substituent can tune the charge ordering, structural stability and thus the lithiation behavior of α-MnO_2. More importantly, this analysis develops key concepts for the rational optimization of 1D tunnel structured materials, enabling higher lithiation potential, increased capacity, and enhanced capacity retention with repeated cycling.

2. Computational Model and Methodology

Spin polarized density functional theory (DFT)[31, 32] calculations were performed using the Vienna *Ab-Initio* Simulation Package (VASP) code.[33, 34] Projector augmented wave (PAW)[35] potentials were used to describe the core electrons with the generalized gradient approximation (GGA) using PBE functionals[36]. The Kohn-Sham one-electron wave functions were expanded by using a plane wave basis set with a kinetic energy cutoff of 400 eV. The Brillouin zone was sampled using a 2 × 2 × 6 k-point grid in the Monkhorst-Pack scheme[37]. Ionic positions were optimized until Hellman-Feynman force on each ion was smaller than 0.01 eV/Å. Soft potentials were used: H, O_GW, Mn_sv_GW, Li_sv_GW, Ti_pv, Cr_pv, V_pv, Ru_pv, and Nb_pv. A Hubbard correction of U = 5.1 eV and J = 1.2 eV was used according to the previous study,[14] showing the experimentally observed anti-ferromagnetic (AFM) nature[38] of α-MnO_2 was accurately simulated using an anisotropic Hubbard J correction.

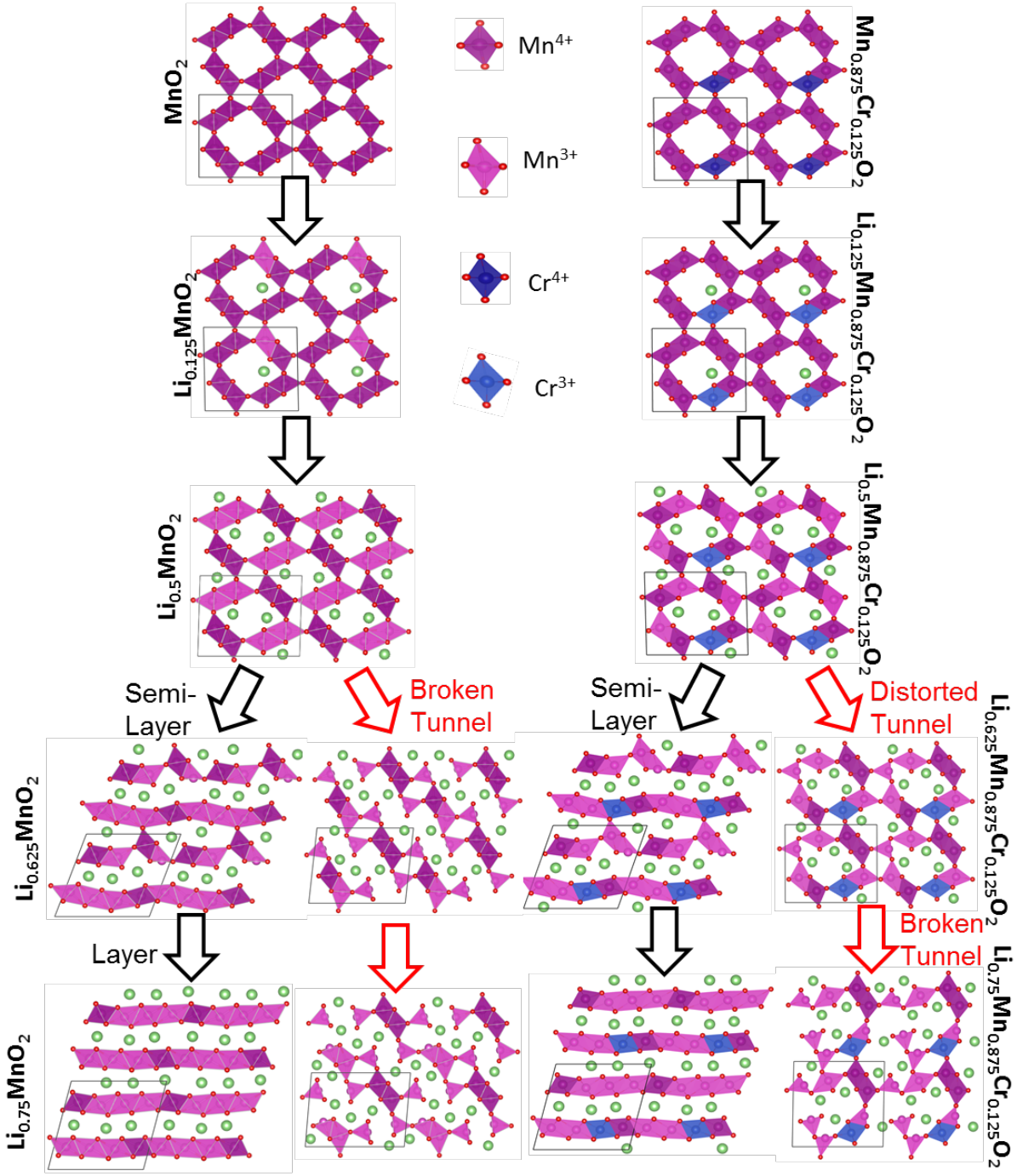

Figure 2. Optimized structures of Li_xMnO_2 and $Li_xMn_{0.875}Cr_{0.125}O_2$ along the kinetically favored broken tunnel pathway and the thermodynamically favored semi-layered pathway (Green: Li; Red: O). The rectangle highlights the supercell considered in the calculation.

α-MnO_2 was described by a Mn_8O_{16} supercell (squared region, Figure 2). The substituted hollandite was described by replacing one Mn atom per supercell of α-MnO_2 with a substituent M

atom, which led to the formation of $Mn_7M_1O_{16}$($Mn_{0.875}M_{0.125}O_2$ in our notation, Figure 1). For $Li_xMn_{0.875}M_{0.125}O_2$, the sequential intercalation of Li from x = 0.125 to x = 0.5, 0.625 0.75 was considered, where various of possible sites were included to map the most stable conformations (Figure S1).

The Li binding energy is defined corresponding to the reaction: $Li_x + Mn_{0.875}M_{0.125}O_2 \rightarrow Li_xMn_{0.875}M_{0.125}O_2$ as $[E(Li_xMn_{0.875}M_{0.125}O_2) - E(Mn_{0.875}M_{0.125}O_2) - xE(Li)]/x$, where $E(Li_xMn_{0.875}M_{0.125}O_2)$, $E(Mn_{0.875}M_{0.125}O_2)$ and E(Li) correspond to the total energy of lithiated state, unlithiated state and metallic Li, respectively. The average lithiation voltage is calculated following the previous studies[39-41] as $-[E(Li_nMn_8M_1O_{16}) - E(Mn_8M_1O_{16}) - nE(Li)]/nF$, where n is the number of Li in the supercell and F is Faraday's constant.

3. Results and Discussion

3.1 Unsubstituted α-MnO_2

Unsubstituted α-MnO_2 was studied here as a benchmark for comparison with the substituted α-MnO_2. For the pristine α-MnO_2, the current calculation well described the lattice, the band gap as well as the anti-ferromagnetic (AFM) C2 ordering reported previously (Figure 1A and see SI). Under lithiation conditions, the 5-coordinated 8h site is preferred for the Li intercalation up to x = 0.5 in Li_xMnO_2 (Figure 2), and the average binding energy of each Li is lowered going from -0.35 eV/$Li_{0.125}MnO_2$ to -0.38 eV/$Li_{0.5}MnO_2$ (Figure S1), which is consistent with the previous DFT calculations.[4, 24] The initial lithiation at x = 0.125 also causes a 2% volume expansion, consistent with the previous studies,[14, 24] though the a/b lattice ratio remains unchanged (Figures 3A,B). At x = 0.5, the volume expands significantly by 7%, and the a/b lattice ratio significantly increases to 1.26 (Figure 3A, B). A previous report[24] also found an increase in the a/b ratio from 1 to the maximum 1.20 at $Li_{0.5}MnO_2$, suggesting that distortions in excess of 1.20 could indicate the risk of tunnel wall breakage. Nonetheless, the tunnel structure remains at $Li_{0.5}MnO_2$ as observed previously theoretically[4, 24] and experimentally.[42] The electron donated by the intercalated Li is localized and results in the reduction of a neighboring Mn ion centered octahedron (reduced Mn in our notation) (Figures 2 and 4). The corresponding concentration is increased from 12.5% at x = 0.125 to 50% at x = 0.5.

There is no generally accepted descriptor to well describe the tunnel stability for α-MnO_2. To quantify the degree of Jahn-Teller distortion, Van Vleck[14, 43] proposed to use the Q3 metric, which relied only on the bond lengths of the ligands and described the square planar distortion from crystal field theory.[43] The method of calculating Q3 in this paper is shown in Figure S2. In term of the Q3 metric, which relies only on the bond lengths of the ligands and describes the square planar distortion from crystal field theory (see SI), the reduced Mn octahedra undergo the Jahn-Teller distortion with the increasing Q3 value of 0.47 Å at x = 0.25 and 0.79 Å at x = 0.5 (Figure 3C) and introduce the structural strain responsible for the structural degradation.[24] To partially relieve the structural strain, the reduced Mn pair up via the edge-sharing motif (reduced Mn pair,

in our notation) and align on opposite sides of the tunnel (see $Li_{0.5}MnO_2$ in Figure 2). As will be discussed in additional detail below, such highly distorted and unstable reduced Mn pairs in an edge-sharing conformation likely can act as the precursor for tunnel breakage. In addition, the reduction in the band gap upon lithiation is also observed via the generation of intermediate states at the band gap or on top of the valence bands of α-MnO_2 according to the calculated projected density of states (PDOS, left of Figure 4), consistent with a previous study.[17]

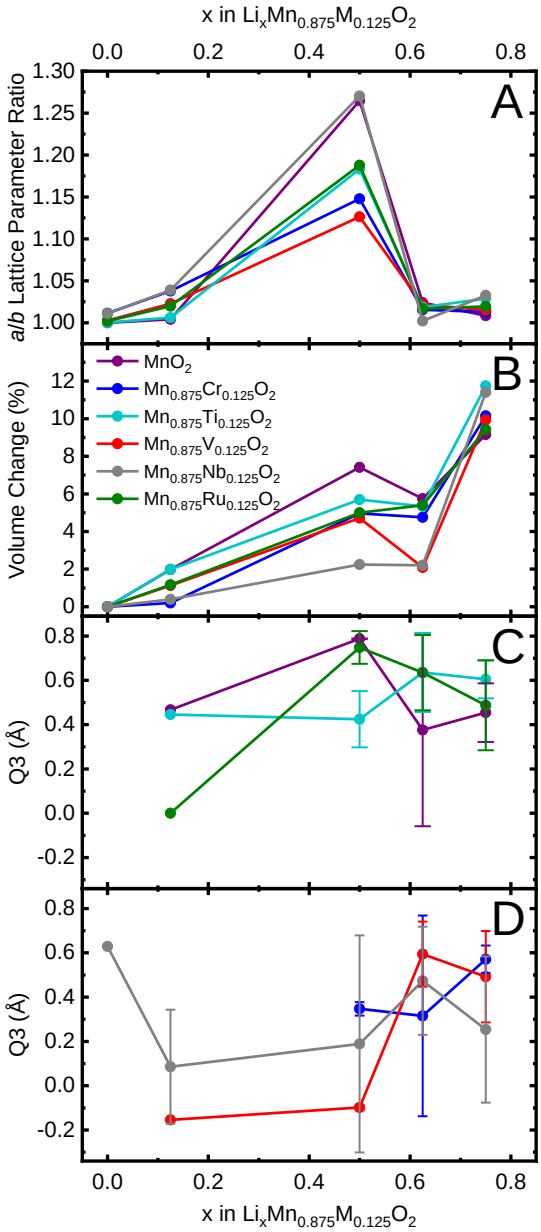

Figure 3. Variation in *a*/*b* lattice parameter ratio (A), volume (B), and (C,D) the average Q3 metrics of Mn octahedra for MnO_2 and $Mn_{0.875}M_{0.125}O_2$ at different lithiation stage and via the semi-layered transition, where the perpendicular bars showed the range of Q3 for the reduced Mn octahedra.

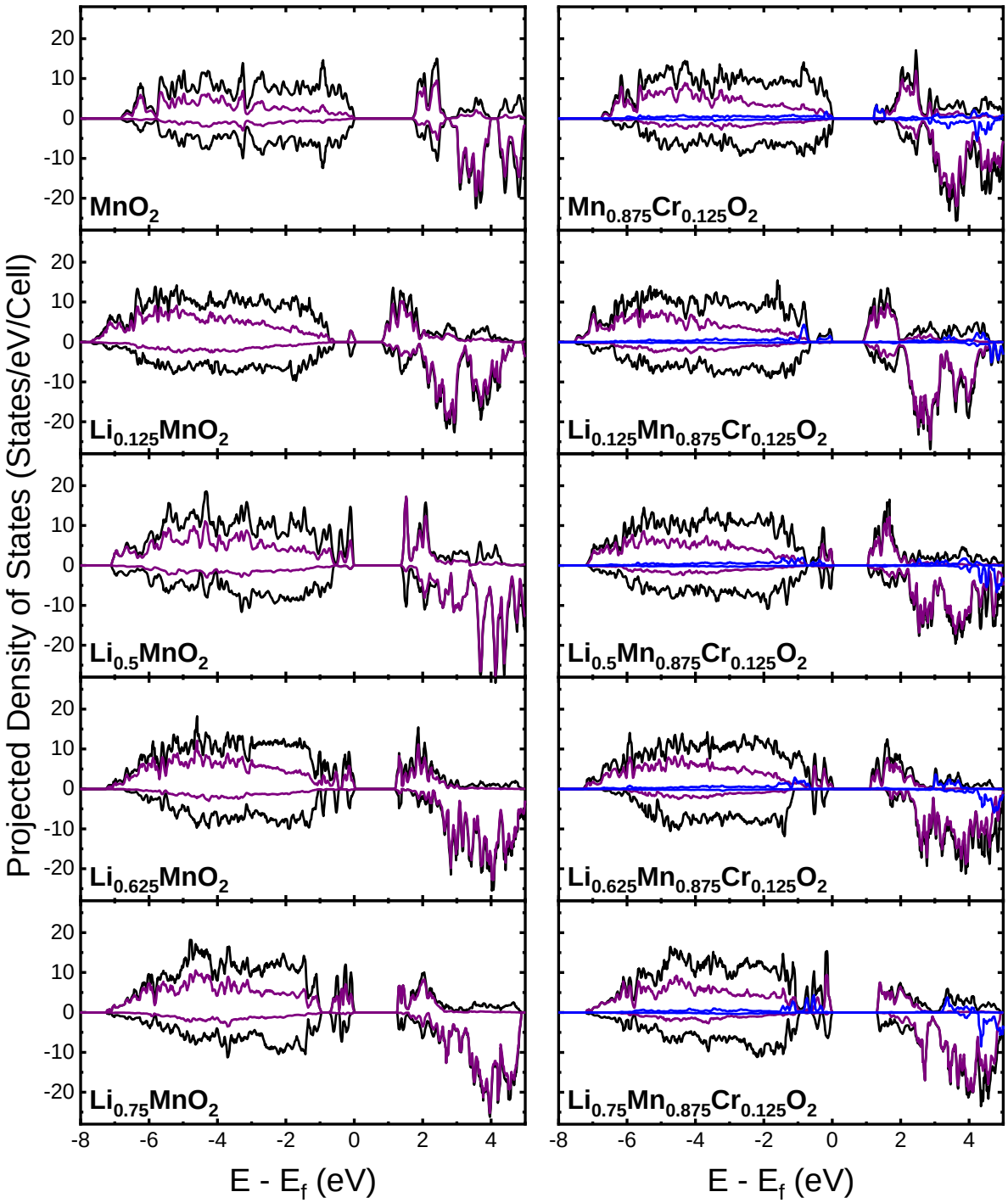

Figure 4. Projected density of states (PDOS) for Li_xMnO_2 (left) and $Li_xMn_{0.875}Cr_{0.125}O_2$ (right) along the broken-tunnel pathway. The total DOS (black line) together with the contribution from Mn (purple) and Cr contribution (blue) were also included.

At x = 0.625, the Li ion inserts into a 4-coordinate 8h′ location (Figure 2), in agreement with the previous calculations.[4, 24] The lithiation at this state leads to the tunnel wall breakage

(broken-tunnel structure in our notation) at the junction of a reduced Mn pair, which transforms the tunneled motif into a rippled layer structure with the Li^+ ions intercalated between the layers (Figure 2). This transformation is facile and occurs spontaneously during the geometry optimization upon insertion of a Li ion (Figure 2). It is also accompanied by weakening of the average binding energy of Li to -0.35 eV/ $Li_{0.625}MnO_2$ (Figure S1), volume expansion to 12%, and an increased a/b lattice ratio to 1.27 (Figure S3).

There is an unpaired reduced Mn in $Li_{0.625}MnO_2$, which is sufficiently distorted with the Q3 metric of 0.55 Å and pairs up with the newly reduced Mn at x = 0.75 (Figure 2). This is accompanied by the loss of one Mn-O bond and a slight increase in Q3 distortion to 0.58 Å and the a/b lattice ratio to 1.33, while the volume expansion and the Li binding energy are hardly changed (Figure S3). The broken-tunnel structure for $Li_{0.75}MnO_2$ is in agreement with previous studies,[4] which was proposed as an intermediate to facilitate the complete loss of the Mn-Mn tunnel network, presumably followed by amorphization.[4] However, the $Li_{0.625}MnO_2$ was not studied previously, which is identified by the current study to be the critical intermediate for initiating the broken-tunnel structure.

Alternatively, $Li_{0.625}MnO_2$ can adopt the semi-layer structure in our notation, which is more thermodynamically favorable by 0.14 eV/$Li_{0.625}MnO_2$ than the corresponding broken-tunnel structure (Figure S1). The semi-layer structure shows similarity to δ-MnO_2 (Figure S4), where the hollandite tunnel structure reorients into parallel layers to hold the Li^+ ions. Layered δ-MnO_2 is the most open structure known for MnO_2 and has been reported to show rapid capacity decay due to its poor electrical conductivity and large volume expansion.[44] Different from δ-MnO_2, in this semi-layer structure there is a corner-sharing link between the layers at the position away from the inserted Li^+ ions and via Mn^{4+}. To accommodate this linkage, the neighboring reduced Mn^{3+} is only 5-coordinate (Figure 2). The energy preference for the semi-layered structure can also be illustrated by the significant reduction in the volume expansion to 6% and decrease in structural distortion with the a/b lattice ratio decreasing back to ~1 (Figures 3A,B). Typically, the positive volume expansion on lithiation is observed, e.g. metal alloys[45], where the structure is gradually distorted during this process. This is indeed that case for Li_xMnO_2 via the broken-tunnel structure (Figure S2B). The negative volume expansion going from the tunneled $Li_{0.5}MnO_2$ to the semi-layered $Li_{0.625}MnO_2$ (Figure 3B) is associated with significant phase transition from the tunneled phase toward the layered phase that is entirely different. The tunnels in δ-MnO_2 provide more empty space, and thus result in larger total volumes than the layered structures (Figure S4).

At x = 0.75, the additional Li insertion results in the reduction of a Mn ion at the corner linking the layers. As a result, the semi-layer structure transforms to a completely layered structure as δ-MnO_2 (Figure 2). Such a layered structure also shows greater stability than the corresponding broken-tunnel structure by -0.13 eV/$Li_{0.75}MnO_2$. This agrees with previous calculations that have shown that the layered structure δ-MnO_2 is more stable than the tunneled α-MnO_2 for $Li_{0.75}MnO_2$.[46] The cell expands to 9%, while the a/b lattice ratio remains around 1 (Figures 3A,B). The Mn^{3+} ions are evenly distributed between the adjacent layers, and the corresponding Q3 distortion is rather small (Figure 3C).

From a thermodynamic perspective, α-MnO_2 favors decomposition into other polymorphs, where the relative stability can be strongly dependent on the intercalated cation type and quantity,[47-49] the solution pH,[50, 51] and water content.[52] According to the DFT calculations the Li^+ ion does not favor the layered structure; yet it is thermodynamically more stable than the tunneled structure at highly lithiated states.[46] Nevertheless, a mechanism for the transition between α and δ phase of MnO_2 has not been studied. Our calculations report for the first time an alternative lithiation pathway involving a transition from the tunneled α-MnO_2-like $Li_{0.5}MnO_2$ to the layered δ-MnO_2-like $Li_{0.75}MnO_2$ structure via the semi-layer intermediate, which is more thermodynamically favorable than the previously proposed via the broken-tunnel intermediate.[4]

Compared to the broken-tunnel structure, the corresponding layer ($Li_{0.75}MnO_2$) structure displays less structural change upon Li^+ insertion (Figures 3 and S3) and more stability. However, kinetically the broken-tunnel structure is more readily accessed than the semi-layer structure, due to more similarity in structure between tunneled $Li_{0.5}MnO_2$ and broken-tunneled $Li_{0.625}MnO_2$. Thus, the broken-tunnel structure likely allows the facile reverse transition on delithiation and the enhanced cyclability. However, along both routes the tunnel breaks at $x > 0.5$. Consequently, neither the broken-tunnel pathway nor the semi-layered structure pathway results in improved structural retention for the unsubstituted MnO_2 material.

3.2 Substituted $Mn_{0.875}M_{0.125}O_2$

For substituted $Mn_{0.875}M_{0.125}O_2$, the $M^{\delta+}$ (Ti^{4+}, V^{4+}, Cr^{4+} and Ru^{4+}) ions maintain a 4+ oxidation state and the substitution does not vary the oxidation state of Mn^{4+} (Figure 1B), which is demonstrated by small Q3 distortion of the corresponding octahedron (Figure 3C,D). However, the effect on the detailed electronic structure differs depending on the M^{n+} substituent. Due to the high stability of Ti^{4+}, the effect on the band gap and the DOS near the Fermi level is rather small (Figure S5), while more significant changes are observed for $Mn_{0.875}M_{0.125}O_2$ ($M^{\delta+}$ = V^{4+}, Cr^{4+}, Ru^{4+}, Figures 4, S6 and S7). For the substituted V^{4+} in $Mn_{0.875}V_{0.125}O_2$, the 3d electrons contribute to the intermediate states on top of the valence states (Figure S6). As a result, the Fermi level is shifted, and the band gap is reduced to 1.39 eV. In this case, the V^{4+} ion acts as a shallow electron donor. Such phenomena have also been observed previously for the doped metal oxides, e.g. N-doped TiO_2.[53, 54] The substituted Cr^{4+} in $Mn_{0.875}Cr_{0.125}O_2$ behaves as an electron acceptor, which contributes to the states on the bottom of the conduction states and reduces the bandgap to 1.28 eV as compared to the unsubstituted MnO_2 (Figure 4). Thus, the Cr^{4+} ion can be reduced more readily than Mn^{4+}. This is due to the half-metallic nature of Cr^{4+} octahedrally coordinated by oxygen atoms in CrO_2 bulk as that in $Mn_{0.875}Cr_{0.125}O_2$, where the major spin-up electrons are metallic, and the minor spin-down electrons are semiconducting. The Ru^{4+} substitution introduces significant electron delocalization into $Mn_{0.875}Ru_{0.125}O_2$, which is associated with the metallic nature of RuO_2 (Figure S7). Consequently, the band gap disappears, where the electron delocalization is centered on the Ru substituent. Different from Ti, V, Cr and Ru substituted $Mn_{0.875}M_{0.125}O_2$, the Nb substituted analog prefers the high oxidation state of 5+ rather than 4+, which results in an electron

transfer and therefore the reduction of the neighboring Mn^{4+} ion to Mn^{3+} (Figure 1C) with the Q3 value as high as 0.6 Å (Figure 3D). Although an intermediate state on top of the valence states is generated (Figure S8) as the case of $Mn_{0.875}V_{0.125}O_2$, the contribution is from the reduced Mn^{3+} rather than Nb^{5+} ions.

During the lithiation process, for $x \leq 0.5$ $Li_xMn_{0.875}M_{0.125}O_2$ behaves in a manner similar to Li_xMnO_2. Each Li^+ ion insertion at the 8h site is an exothermic process (Figures 2, S9-S12), enabling one electron donation to reduce one Mn^{4+}, and introducing a corresponding distortion to the center octahedron. $Mn_{0.875}Cr_{0.125}O_2$ is one of the exceptions, where Cr^{4+} shows higher reduction potential compared to Mn^{4+}. Thus, the amount of reduced Mn^{3+} ions in $Li_xMn_{0.875}Cr_{0.125}O_2$ is less than that in Li_xMnO_2 (Figure 2). Although the reduced Ru^{4+} is also observed on lithiation, the reduction is only partial and always involves the neighboring Mn^{4+} (Figure S11 and see SI) due to the electron delocalization. Thus, more Mn^{3+} ions are observed in $Li_xMn_{0.875}Ru_{0.125}O_2$ than that in Li_xMnO_2 and $Li_xMn_{0.875}M_{0.125}O_2$ (M = Ti, V, Cr). A similar increase in Mn^{3+} is also seen for $Li_xMn_{0.875}Nb_{0.125}O_2$ (Figure S12). With the increasing numbers of Li^+ ions inserted, the cell expands, and the a/b ratio increases significantly at x = 0.5 (Figure 3B), while the tunnel structures remain at this stage with the 3d substituent (M = Ti, Cr, V).

In comparison to the 3d substituents, the 4d substituents (M = Nb, Ru) introduce more significant structural distortion and thus strain to the tunnel due not only to their larger difference in size with Mn but also to the greater population of reduced Mn^{3+} ions. To release the strain and maintain the tunnel structure, the neighboring Mn and Nb octahedra transform from an edge-sharing to a corner-sharing motif (Figure S12); while on Ru substitution, the strong Mn-Ru interaction does not enable the corner-sharing conformation and the tunnel is only partially broken via the reduced Mn pairs (Figure S11). Thus, Ru is not a good substituent, as it decreases the tunnel stability of MnO_2 and results in the tunnel breakage as early as x = 0.5 for $Li_xMn_{0.875}Ru_{0.125}O_2$.

At $x > 0.5$, all substituted systems appear to undergo significant distortion and structural change. The degree of tunnel breakage for $Li_xMn_{0.875}Ru_{0.125}O_2$ increases and the other substituted systems all start to display the tunnel broken at different levels. Following the same principle as that for unsubstituted α-MnO_2, the tunnel breakage of $Li_xMn_{0.875}Ru_{0.125}O_2$ strongly depends on the formation of reduced Mn pairs during the lithiation. As the case of α-MnO_2, the Li intercalation of $Li_xMn_{0.875}Ru_{0.125}O_2$ via the broken-tunnel route introduces more structural distortion and is not thermodynamically as favorable as that via the currently identified layered route; yet, kinetically it is more facile and helps to promote the cyclability.

With the increase in x from 0.5 to 0.625, the broken-tunnel structures are formed spontaneously for $Li_{0.625}Mn_{0.875}M_{0.125}O_2$ (M = Ti, V) during the geometry optimization. At x = 0.625, 62.5% of Mn^{4+} are reduced and the newly reduced Mn^{3+} octahedron is located at the edge-sharing position with either the $M^{\delta+}$ octahedron for M = V or the non-reduced Mn^{4+} octahedron for M = Ti (Figures S9 and S10). As is the case of $Li_{0.625}MnO_2$ and $Li_{0.5}Mn_{0.875}Ru_{0.125}O_2$, the tunnel always cleaves at the junction of reduced Mn pairs for $Li_{0.625}Mn_{0.875}M_{0.125}O_2$ (M = Ti, V). In contrast, the substitution by Cr or Nb can completely or partially hinder the tunnel breakage at high lithiation states ($x > 0.5$) and formation of broken-tunnel structure at x = 0.625. The reason

appears to be associated with the tunnel-stabilization introduced by the substituents. In $Li_{0.625}Mn_{0.875}Cr_{0.125}O_2$ the reduced Mn is only 50%, which is lower than $Li_{0.625}MnO_2$ and $Li_{0.625}Mn_{0.875}M_{0.125}O_2$ (M = Ti, V). It thus hinders the formation of reduced Mn pairs. In addition, the Jahn-Teller distortion of the reduced Cr^{3+} octahedron is not observed. Both features help to stabilize the tunnel at x = 0.625 (Figure 2).

For $Li_{0.625}Mn_{0.875}Nb_{0.125}O_2$, the structural flexibility of Nb octahedra via the corner-sharing binding motif enables the release of strain for the interacting reduced Mn^{3+} octahedra (Figure S12). As a result, the low Q3 metric (see SI) is observed even with 75% of reduced Mn^{3+} ions. In this case, the tunnel partially breaks via one reduced Mn pair previously formed in $Li_{0.5}Mn_{0.875}Nb_{0.125}O_2$, which is further away from the Nb ion and is more distorted with a Q3 of 0.67 Å and 0.73 Å prior to the loss of the Mn-O bonds. At state of lithiation, the other metal ion pairs stay connected. Upon increasing lithiation from x = 0.625 to x = 0.75, the newly reduced Mn octahedron forms the edge-sharing pair with the M octahedron for M = V, Ru, while the broken-tunnel structure remains largely intact (Figures S10 and S11). This is also the case for $Li_{0.75}Mn_{0.875}Ti_{0.125}O_2$. However, one of the MnO_5 square pyramids is further reduced to Mn^{2+}, and the amount of reduced Mn remains the same as that at x = 0.625 (Figure S9). As a result, the lattice changes slightly with the increase in volume expansion (≤ 2%), and the decrease in the a/b ratio (≤ 0.03, Figure S3). For M = Cr, the newly reduced Mn ions are present in the form of reduced Mn pairs, which leads to the Mn-O bond cleavage to form a MnO_5 square pyramid and therefore partial tunnel breakage (Figure 2). In the case M = Nb, the partially broken-tunnel at x = 0.625 remains (Figure S12). Given that, both Cr and Nb substitutions likely promote the stability of the tunnel structure of Li_xMnO_2 at high lithiation.

In a similar manner to $Li_{0.625}MnO_2$, $Li_{0.625}Mn_{0.875}M_{0.125}O_2$ (M = Ti, V, Cr, Ru) adopts the semi-layer structure, where the layers can be connected via either the $M^{\delta+}$ octahedron, the non-reduced Mn^{4+} octahedron and/or reduced $Mn^{3+/2+}$ octahedron (Figures 2 and S9-S11). Again, the transition of $Li_{0.5}Mn_{0.875}M_{0.125}O_2$ to the semi-layered structure is thermodynamically more preferred than the transition to the broken-tunnel structure by 0.22 eV/$Li_{0.625}Mn_{0.875}Ti_{0.125}O_2$, 0.27 eV/$Li_{0.625}Mn_{0.875}V_{0.125}O_2$, 0.22 eV/$Li_{0.625}Mn_{0.875}Cr_{0.125}O_2$, 0.08 eV/$Li_{0.625}Mn_{0.875}Ru_{0.125}O_2$ and 0.15 eV/$Li_{0.625}Mn_{0.875}Nb_{0.125}O_2$. The transition is accompanied by a unit cell contraction and a significant decrease in the a/b ratio (Figure 3A,B). Once the layered structure is formed, the distortion of reduced $Mn^{3+/2+}$ octahedra for all the cases considered is relatively similar and the variation in the Q3 metrics from one system to the next is small (Figure 3C,D). For $Li_{0.625}Mn_{0.875}Nb_{0.125}O_2$, the semi-layer structure involves more corner-sharing links between the layers than the other cases via the reduced Mn^{2+} and Nb^{5+} ions (Figure S12). Additionally, a broken Mn layer structure is observed for $Li_{0.625}Mn_{0.875}Nb_{0.125}O_2$ (Figure S13), which indicates slightly higher stability than the semi-layered structure by 0.04 eV/$Li_{0.625}Mn_{0.875}Nb_{0.125}O_2$. At x = 0.75, the semi-layer structure of $Li_{0.625}Mn_{0.875}M_{0.125}O_2$ (M = Ti, V, Cr, Ru, Nb) transforms to the δ-MnO_2-like layered conformation. The link between the neighboring layers disappears on Li intercalation and the Li^+ ions are well dispersed between the layers (Figures 2 and S8-S11). This layered conformation is energetically more favorable than the corresponding broken-tunnel structure by

0.20 eV/$Li_{0.625}Mn_{0.875}Ti_{0.125}O_2$, 0.06 eV/$Li_{0.625}Mn_{0.875}V_{0.125}O_2$, 0.17 eV/$Li_{0.625}Mn_{0.875}Cr_{0.125}O_2$ and 0.07 eV/$Li_{0.625}Mn_{0.875}Ru_{0.125}O_2$.

According to the previous studies, the layered structure is more favorable than the tunneled conformation for MnO_2[7, 8]. The present DFT calculations also show the thermodynamically preference to the layer-like structure for $Li_xMn_{0.875}M_{0.125}O_2$ at x > 0.5, e.g. broken-tunnel and semi-layer. However, experimentally to enable the high cyclability α-MnO_2 is typically cycled to x = 0.5 to avoid the tunnel breaking and formation of the layer-like structure at higher lithiation states[5, 16, 20]. The focus of current study is the tuning effect of substitution. Indeed, as demonstrated above, the Cr- or Nb-substitution allows the maintaining of tunnel structure of α-MnO_2 at the increased in the degree of lithiation to x = 0.625.

3.3 Lithiation Potential

The lithiation behavior was estimated according to the calculated open circuit voltage. We note that the calculated initial average voltage for α-MnO_2 (2.81 V, Figure 5) is lower than the experimental observations (> 3.0 V)[21,42] and prior theoretical calculations (3.51 V[24] and 3.36 V[4]). The difference is due to the small supercell used in our calculations, which limits the description of Li_xMnO_2 at low Li concentration (x < 0.125) and the possible distributions of Li at low concentrations. However, the results here are used in a comparative manner to address the difference across the series of Li_xMnO_2 to $Li_xMn_{0.875}M_{0.125}O_2$ which is the focus of this study.

At the initial lithiation stage (x = 0.125), all of the transition metal substituted $Mn_{0.875}M_{0.125}O_2$ materials show higher voltage than MnO_2, where the substitution helps to stabilize the lithiated tunnel structure and therefore the Li binding by reducing the Jahn-Teller distortion in the reduced Mn or M octahedra (Figure 3C,D). The $Mn_{0.875}Cr_{0.125}O_2$ displays the highest potential of the group with an average voltage of 3.59 V (Figure 5). This is followed by $Mn_{0.875}V_{0.125}O_2$ (3.11 V) > $Mn_{0.875}Nb_{0.125}O_2$ (3.03 V) > $Mn_{0.875}Ti_{0.125}O_2$ (2.93 V) > $Mn_{0.875}Ru_{0.125}O_2$ (2.91 V) in a decreasing sequence. The higher reduction potential of Cr^{4+} compared to Mn^{4+} (right of Figure 4) makes the substituted Cr act as an electron acceptor, and the small distortion of a reduced Cr octahedron enhances the stability of $Li_{0.125}Mn_{0.875}Cr_{0.125}O_2$. Although the substituted Ru^{4+} also acts as an electron acceptor (Figure S7), it is not as strongly preferred as Cr^{4+}.[55, 56] At the lithiation level of x = 0.5, $Mn_{0.875}Cr_{0.125}O_2$ again displays the highest lithiation voltage of the group with a value of 3.15 V, (Figure 5). Notably, the voltages provided by the other $Mn_{0.875}M_{0.125}O_2$ substituted materials are even lower than $Li_{0.5}MnO_2$.

At x = 0.625, $Mn_{0.875}V_{0.125}O_2$ indicates the highest potential among the systems via the broken-tunnel structure (Figure S13), while at x = 0.75 $Mn_{0.875}Nb_{0.125}O_2$ provides a slightly higher potential. By adopting the semi-layer structure, the advantage of Cr substitution at x ≤ 0.5 over the other substituents and the non-substituted systems remains. As the lithiation level increases, $Mn_{0.875}Cr_{0.125}O_2$ displays the highest potential of 3.13 V when x = 0.625 and 3.08 V at x = 0.75.

However, the difference in potential among the studied systems is smaller when x = 0.625 and x = 0.75 as compared to those when x ≤ 0.5 (Figures 5 and S14).

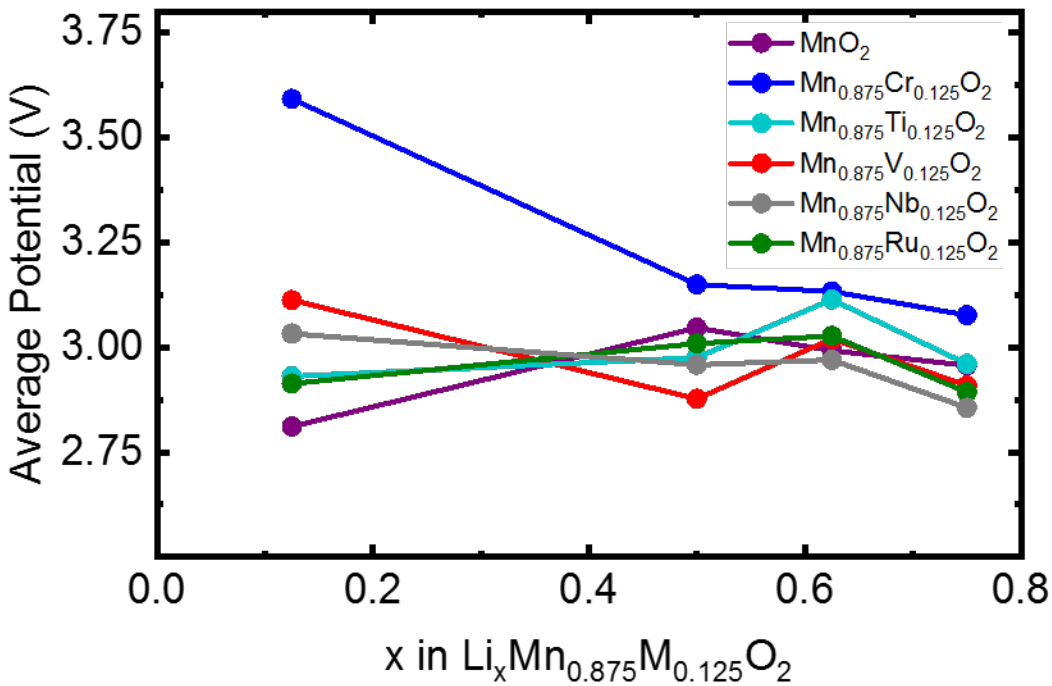

Figure 5. Average lithiation potentials of MnO_2 and $Mn_{0.875}M_{0.125}O_2$ via the semi-layered transition.

According to our calculations, all $Mn_{0.875}M_{0.125}O_2$ systems studied enable an increase in the voltage for the initial lithiation at x = 0.125. Cr is the only substituent that shows higher voltage not only at the initial stage of lithiation at x ≤ 0.5, but also when x > 0.5 via the semi-layer transition. The origin of the effect is associated with the unique capability of Cr as an electron acceptor. The substituted Cr^{4+} generates the lowest unoccupied states, being more readily reduced than Mn^{4+} and the other M ions where it can accept the electrons donated from the inserted Li via the facile $Cr^{4+} \rightarrow Cr^{3+}$ transformation. Our results highlight the importance of reduction potential relative of the substituent from 4+ to 3+ to the Mn centers to increase the lithiation potential of the MnO_2 based structure. Yet, we have to note, despite the slightly higher potential for the semi-layer structure than the broken-tunnel structure for $Li_xMn_{0.875}Cr_{0.125}O_2$ at x > 0.5 the transition from the broken-tunnel to the semi-layer may not be kinetically accessible. As demonstrated in section 3.4, it is the higher cyclability, which makes the lithiation of $Mn_{0.875}M_{0.125}O_2$ via the broken-tunnel transition more attractive than that via the semi-layer transition.

3.4 Cyclability and Capacity

Good cyclability depends on the high stability of the tunnel structure and smooth transition from one lithiated state to the next during lithiation, which likely facilitates the reverse, delithiation, process. The retention of the high theoretical capacity of MnO_2, on the other hand, requires the enhancement in structural stability, particularly the tunnel structure at highly lithiated states (x > 0.5). The structural stability was previously described by the degree of the tunnel breakage, the lattice a/b ratio, the structural distortion in term of cell volume, or the Q3 metric for the Jahn-Teller distortion (see SI). In term of tunnel breakage, all $Li_xMn_{0.875}M_{0.125}O_2$ systems can maintain the tunnel structure up to a lithiation level of x = 0.5 (Figures 2 and S9-S12). At x = 0.625, the tunnel breaks for most of the substituted systems via the broken-tunnel route, where the insertion of Li results in a spontaneous transition of the tunnel structure to a broken-tunnel conformation (Figures 2 and S9-S12). $Li_{0.5}Mn_{0.875}Cr_{0.125}O_2$ is the only system to allow the tunnel structure to remain at x = 0.625 (Figure 2). The Nb-substituted system also enhances structural stability, which enables only partial tunnel breakage (Figure S12). Upon further lithiation to x = 0.75, the tunnel wall of Cr-substituted system is partially broken, while no additional bond breakage is observed by Nb substitution. Retaining the tunnel structures at highly lithiated states, x = 0.625 and x = 0.75, provides the opportunity for a ~25% or even 50% increased capacity over x = 0.5, respectively. When the semi-layered route is followed, the tunnel breaks for all the systems studied at x = 0.625and thus the substitution does not aid in alleviating the capacity degradation of MnO_2.

The variation in the a/b ratio, cell volume and Q3 with x is clearly shown for both Li_xMnO_2 and $Li_xMn_{0.875}M_{0.125}O_2$ studied (Figure 3). The Li intercalation causes the asymmetric volume changes, which is demonstrated by the higher a/b ratio than that of pristine α-MnO_2. Such structural variation was attributed to the Jahn-Teller distortions associated with the reduced Mn ions, Mn^{3+}, and was quantified by the Q3 metric[14, 43]. For Li_xMnO_2, all three variables are likely associated with the tunnel breakage, which is demonstrated by a large a/b ratio, the significant volume expansion or emergence of large Q3 value, in consistent with previous studies[14, 24, 43]. However, no strict correlation is observed for the substituted systems. For instance, $Li_{0.5}Mn_{0.875}Nb_{0.125}O_2$ displays the least volume change on lithiation among the substituted systems studied (Figures 3B), but the corresponding a/b ratio is the highest (Figure 3A). In addition, such a high a/b ratio does not result in the tunnel breakage as previously observed for MnO_2.[24] As the Nb is highly oxidized and there is a large difference in size between Nb and Mn, the relatively weak Nb-Mn interaction enables the formation of the corner-sharing Nb octahedron (Figure S11). It also results in the formation of the MnO_5 square pyramid, which enhances the structural flexibility in order to accommodate Li insertion with the least effect on volume. It is the MnO_5 square pyramid which introduces the high a/b ratio. This is beyond the description of Q3, which is defined only to describe the common MnO_6 octahedron. In this case, the substituted metal ions can behave differently from Mn ions, which cannot be well described by the three variables proposed for Li_xMnO_2. Nevertheless, none of them can clearly pinpoint the origin of the tunnel breakage, while according to our calculations, the formation of edge-sharing reduced Mn pairs is the key to enable the open tunnel.

In terms of the structural similarity of $Li_xMn_{0.875}M_{0.125}O_2$, the broken-tunnel transition enables a smooth transition from the tunneled (x = 0.5) to the broken-tunnel (x = 0.625) conformation. By comparison, the transition to the semi-layered structure undergoes more significant structural changes. It means that the semi-layer transition can be kinetically more difficult to access than the broken-tunnel transition during lithiation, even though it is thermodynamically more favorable. Additionally, it also likely hinders the reverse, delithiation, process. Thus, the broken-tunnel transition is more desirable than the semi-layered transition for enhancing the long term cyclability.

According to our calculations, the Cr and Nb substituents will result in improved capacity retention with cycling and greater capacity than the other substituents via the broken-tunnel transition which is kinetically favorable for lithiation and likely delithiation. According to our results, there is no clear dependence of tunnel breakage on the volume change, the a/b ratio or the Q3 metric. Instead, three factors were identified as key indicators to deter the tunnel breakage and enhance structural stability during the lithiation. The first is to avoid the formation of reduced Mn pairs in an edge-sharing conformation, which introduces significant structural distortion and is likely the precursor for tunnel breakage. The substituted Cr^{4+} achieves this by acting as an active electron acceptor and is reduced more readily than Mn^{4+} during initial lithiation. In this way, the number of reduced Mn centers within the tunnel structure is limited (Figure 2). In addition, the rigidity of the reduced Cr octahedra also helps to prevent the formation of reduced Mn pairs. The second indicator is the release of the strain imposed on the tunnel wall by Li intercalation. This is the case demonstrated by the Nb-substituted system. Although the Nb^{4+} center acts as an electron donor and favors the formation of reduced Mn^{3+} ions, the weak interaction between the Nb^{5+} octahedra and the Mn^{3+} octahedra enables the structural preference to the corner-sharing conformation together with the formation of MnO_5 tetrahedra rather than the edge-sharing (Figure S12). This helps in alleviating the structural strain introduced by the Mn^{3+}octahedra, so that the Li insertion can be effectively accommodated by the tunnel structure. As a third consideration, the enhancement in stability of the broken-tunnel structure relative to the corresponding semi-layered or layered structure is important to tune the lithiation toward following the broken-tunnel path and thus promote improved capacity retention with that pathway.

4. Conclusion

In summary, a bottom-up screening using DFT calculations specifically identifies Cr to be the transition metal substituent among the $Mn_{0.875}M_{0.125}O_2$ (M = Ti, V, Cr, Nb, Ru) series capable of greatly increasing the lithiation potential of MnO_2 not only at low (x < 0.5), but also at high (x > 0.5) Li concentrations. Wherein, a new lithiation pathway via a semi-layer transition is discovered, which is thermodynamically more preferred, but kinetically less feasible than the previously reported broken-tunnel transition. In terms of the cyclability, again the substitution by Cr is the most effective among all studied, enabling retention of the tunnel structure completely up to x = 0.625 with only partial tunnel breakage observed at x = 0.75 via the broken-tunnel transition.

The Nb-substitution helps to stabilize the partially broken tunnel at x = 0.625 and x = 0.75. In contrast for α-MnO_2 tunnel breakage occurs at x =0.5. Thus, the stabilized tunnel structures at x = 0.625 and x = 0.75 for the transition metal substituted α-MnO_2 structures provide the opportunity for a ~25% or even 50% increased capacity over x = 0.5, respectively.

Finally, our study provides new insights into advancing general principles for improving the structural stability at higher levels of lithiation for α-MnO_2 via partial substitution of Mn by transition metal, M. To promote the lithiation potential, the substituent should be an active electron acceptor, capable of facilitating the $M^{4+} \rightarrow M^{3+}$ reduction more readily than $Mn^{4+} \rightarrow Mn^{3+}$. In order to promote the cyclability, an effective substituent should stabilize the tunnel structure during the lithiation by minimizing the formation of reduced Mn pairs or/and alleviating the strain imposed on the tunnel wall via the weak M-Mn interaction and the loosely corner-sharing conformation. In addition, in case that the tunnel is broken on lithiation, the transition from the tunnel structure via the broken-tunnel path rather than the semi-layer path should be favored by substitution. The increased stability of the α-MnO_2 structure through transition metal substitution of the Mn centers in the tunnel walls provides a new paradigm for material design leading to higher delivered capacities with increased capacity retention.

Supporting Information

Atomic and electronic structures involved in the discharging process for substituted MnO_2. Lithiation potential at different stages and the corresponding variation in volume, a/b ratio and Q3 value. This material is available free of charge via the Internet at http://pubs.acs.org.

Author Information

Corresponding author
* Email: kenneth.takeuchi.1@stonybrook.edu (K. J. Takeuchi), pingliu3@bnl.gov (P. Liu)

Conflict of Interest

The authors declare no conflict of interest

Acknowledgements

This work was carried out at Brookhaven National Laboratory (BNL), and was funded as part of the Center for Mesoscale Transport Properties (m2M), an Energy Frontier Research Center (EFRC) supported by the U.S. Department of Energy, Office of Science, Basic Energy Sciences, under Award No. DE-SC0012673. The DFT calculations were performed using computational resources at the Center for Functional Nanomaterials, a U.S. DOE Office of Science Facility, and the Scientific Data and Computing Center, a component of the Computational Science Initiative at BNL under Contract No. DE-SC0012704. The authors would also like to thank Stony Brook Research Computing and Cyberinfrastructure, and the Institute for Advanced Computational Science at Stony Brook University for access to the high-performance SeaWulf computing system, which was made possible by a $1.4M National Science Foundation grant (#1531492).

EST acknowledges the generous support of William and Jane Knapp through the Knapp Chair of Energy and the Environment.

Reference

1. Yang, Z.; Ford, D. C.; Park, J. S.; Ren, Y.; Kim, S.; Kim, H.; Fister, T. T.; Chan, M. K. Y.; Thackeray, M. M., Probing the Release and Uptake of Water in α-$MnO_2 \cdot xH_2O$. *Chem. Mater.* **2017,** *29*, 1507-1517.
2. Pigliapochi, R.; Seymour, I. D.; Merlet, C.; Pell, A. J.; Murphy, D. T.; Schmid, S.; Grey, C. P., Structural Characterization of the Li-Ion Battery Cathode Materials $LiTi_xMn_{2-x}O_4$ ($0.2 \leq x \leq 1.5$): A Combined Experimental 7Li NMR and First-Principles Study. *Chem. Mater.* **2018,** *30*, 817-829.
3. Zhang, W.; Cupid, D. M.; Gotcu, P.; Chang, K.; Li, D.; Du, Y.; Seifert, H. J., High-Throughput Description of Infinite Composition–Structure–Property–Performance Relationships of Lithium–Manganese Oxide Spinel Cathodes. *Chem. Mater.* **2018,** *30*, 2287-2298.
4. Tompsett, D. A.; Islam, M. S., Electrochemistry of Hollandite α-MnO2: Li-Ion and Na-Ion Insertion and Li2O Incorporation. *Chem. Mater.* **2013,** *25*, 2515-2526.
5. Housel, L. M.; Wang, L.; Abraham, A.; Huang, J.; Renderos, G. D.; Quilty, C. D.; Brady, A. B.; Marschilok, A. C.; Takeuchi, K. J.; Takeuchi, E. S., Investigation of α-MnO_2 Tunneled Structures as Model Cation Hosts for Energy Storage. *Acc. Chem.Res.* **2018,** *51*, 575-582.
6. Julien, C.; Mauger, A., Nanostructured MnO_2 as Electrode Materials for Energy Storage. *Nanomaterials* **2017,** *7*, 396.
7. Post, J. E., Manganese Oxide Minerals: Crystal Structures and Economic and Environmental Significance. *Proc. Nat. Acad. Sci.* **1999,** *96*, 3447-3454.
8. Li, Y.-F.; Liu, Z.-P., Active Site Revealed for Water Oxidation on Electrochemically Induced δ-MnO_2: Role of Spinel-to-Layer Phase Transition. *J. Am. Chem. Soc.* **2018,** *140*, 1783-1792.
9. Poyraz, A. S.; Song, W.; Kriz, D.; Kuo, C.-H.; Seraji, M. S.; Suib, S. L., Crystalline Mesoporous $K_{2-x}Mn_8O_{16}$ and ε-MnO_2 by Mild Transformations of Amorphous Mesoporous Manganese Oxides and Their Enhanced Redox Properties. *ACS Appl. Mater. Interfaces* **2014,** *6*, 10986-10991.
10. Wei, W.; Cui, X.; Chen, W.; Ivey, D. G., Manganese Oxide-based Materials as Electrochemical Supercapacitor Electrodes. *Chem. Soc. Rev.* **2011,** *40*, 1697-1721.
11. Cheng, F.; Zhao, J.; Song, W.; Li, C.; Ma, H.; Chen, J.; Shen, P., Facile Controlled Synthesis of MnO_2 Nanostructures of Novel Shapes and Their Application in Batteries. *Inorg. Chem.* **2006,** *45*, 2038-2044.
12. Johnson, C. S.; Dees, D. W.; Mansuetto, M. F.; Thackeray, M. M.; Vissers, D. R.; Argyriou, D.; Loong, C. K.; Christensen, L., Structural and Electrochemical Studies of α-Manganese Dioxide (α-MnO_2). *J. Power Sources* **1997,** *68*, 570-577.
13. Yang, Z.; Trahey, L.; Ren, Y.; Chan, M. K. Y.; Lin, C.; Okasinski, J.; Thackeray, M. M., In Situ High-Energy Synchrotron X-ray Diffraction Studies and First Principles Modeling of α-MnO_2 Electrodes in Li–O_2 and Li-Ion Coin Cells. *J. Mater. Chem. A* **2015,** *3*, 7389-7398.
14. Kaltak, M.; Fernández-Serra, M.; Hybertsen, M. S., Charge Localization and Ordering in $A_2Mn_8O_{16}$ Hollandite Group Oxides: Impact of Density Functional Theory Approaches. *Phys. Rev. Mater.* **2017,** *1*, 075401.

15. Yuan, Y.; Nie, A.; Odegard, G. M.; Xu, R.; Zhou, D.; Santhanagopalan, S.; He, K.; Asayesh-Ardakani, H.; Meng, D. D.; Klie, R. F.; et al., Asynchronous Crystal Cell Expansion during Lithiation of K^+-Stabilized α-MnO_2. *Nano Lett.* **2015,** *15*, 2998-3007.
16. Huang, J.; Housel, L. M.; Quilty, C. D.; Brady, A. B.; Smith, P. F.; Abraham, A.; Dunkin, M. R.; Lutz, D. M.; Zhang, B.; Takeuchi, E. S.; et al., Capacity Retention for (De)lithiation of Silver Containing α-MnO_2: Impact of Structural Distortion and Transition Metal Dissolution. *J. Electrochem. Soc.* **2018,** *165*, A2849-A2858.
17. Young, M. J.; Holder, A. M.; George, S. M.; Musgrave, C. B., Charge Storage in Cation Incorporated α-MnO_2. *Chem. Mater.* **2015,** *27*, 1172-1180.
18. Johnson, C. S.; Thackeray, M. M., Ammonia- and Lithia-Doped Manganese Dioxide for 3 V Lithium Batteries. *J. Power Sources* **2001,** *97-98*, 437-442.
19. Zhai, D.; Li, B.; Xu, C.; Du, H.; He, Y.; Wei, C.; Kang, F., A Study on Charge Storage Mechanism of α-MnO_2 by Occupying Tunnels with Metal Cations (Ba^{2+}, K^+). *J. Power Sources* **2011,** *196*, 7860-7867.
20. Poyraz, A. S.; Huang, J.; Cheng, S.; Wu, L.; Tong, X.; Zhu, Y.; Marschilok, A. C.; Takeuchi, K. J.; Takeuchi, E. S., Tunnel Structured α-MnO_2 with Different Tunnel Cations (H^+, K^+, Ag^+) as Cathode Materials in Rechargeable Lithium Batteries: The Role of Tunnel Cation on Electrochemistry. *J. Electrochem. Soc.* **2017,** *164*, A1983-A1990.
21. Poyraz, A. S.; Huang, J.; Pelliccione, C. J.; Tong, X.; Cheng, S.; Wu, L.; Zhu, Y.; Marschilok, A. C.; Takeuchi, K. J.; Takeuchi, E. S., Synthesis of Cryptomelane Type α-MnO_2 ($K_xMn_8O_{16}$) Cathode Materials with Tunable K^+ Content: the Role of Tunnel Cation Concentration on Electrochemistry. *J. Mater. Chem. A* **2017,** *5*, 16914-16928.
22. Wu, L.; Xu, F.; Zhu, Y.; Brady, A. B.; Huang, J.; Durham, J. L.; Dooryhee, E.; Marschilok, A. C.; Takeuchi, E. S.; Takeuchi, K. J., Structural Defects of Silver Hollandite, Ag_x Mn_8O_y, Nanorods: Dramatic Impact on Electrochemistry. *ACS nano* **2015,** *9*, 8430-8439.
23. Xu, F.; Wu, L.; Meng, Q.; Kaltak, M.; Huang, J.; Durham, J. L.; Fernandez-Serra, M.; Sun, L.; Marschilok, A. C.; Takeuchi, E. S.; Takeuchi, K. J.; et al., Visualization of Lithium-Ion Transport and Phase Evolution Within and Between Manganese Oxide Nanorods. *Nature Commun.* **2017,** *8*, 15400.
24. Ling, C.; Mizuno, F., Capture Lithium in αMnO_2: Insights from First Principles. *Chem. Mater.* **2012,** *24*, 3943-3951.
25. Cai, J.; Liu, J.; Willis, W. S.; Suib, S. L., Framework Doping of Iron in Tunnel Structure Cryptomelane. *Chem. Mater.* **2001,** *13*, 2413-2422.
26. Polverejan, M.; Villegas, J. C.; Suib, S. L., Higher Valency Ion Substitution into the Manganese Oxide Framework. *J. Am. Chem. Soc.* **2004,** *126*, 7774-7775.
27. Tang, X.; Li, Y.; Chen, J.; Xu, Y.; Shen, W., Synthesis, Characterization, and Catalytic Application of Titanium–Cryptomelane Nanorods/Fibers. *Microporous and Mesoporous Mater.* **2007,** *103*, 250-256.
28. Hashem, A. M.; Abuzeid, H. M.; Mikhailova, D.; Ehrenberg, H.; Mauger, A.; Julien, C. M., Structural and Electrochemical Properties of α-MnO_2 Doped with Cobalt. *J. Mater. Sci.* **2012,** *47*, 2479-2485.
29. Ching, S.; Carmichael, J. R.; Eichelberger, L. A.; Kriz, D. A.; Alley, K. A.; Jackvony, S. E., Influence of Fe, Cu, V, and Ce Doping on Morphology and Catalytic Activity of Amorphous Manganese Oxide Hollow Spheres. *Polyhedron* **2016,** *114*, 205-212.
30. Vladimir, T.; Anton, H. H.; Tejs, V., Computational Screening of Doped α-MnO_2 Catalysts for the Oxygen Evolution Reaction. *ChemSusChem* **2018,** *11*, 629-637.

31. Hohenberg, P.; Kohn, W., Inhomogeneous Electron Gas. *Phys. Rev. B* **1964,** *136*, B864-B871.
32. Kohn, W.; Sham, L. J., Self-Consistent Equations Including Exchange and Correlation Effects. *Phys. Rev.* **1965,** *140* , A1133-a1138.
33. Kresse, G.; Furthmuller, J., Efficiency of Ab-Initio Total Energy Calculations for Metals and Semiconductors using A Plane-Wave Basis Set. *Comp. Mater. Sci.* **1996,** *6*, 15-50.
34. Kresse, G.; Furthmuller, J., Efficient Iterative Schemes for Ab Initio Total-Energy Calculations using A Plane-Wave Basis Set. *Phys. Rev. B* **1996,** *54*, 11169-11186.
35. Blochl, P. E., Projector Augmented-Wave Method. *Phys. Rev. B* **1994,** *50*, 17953-17979.
36. Perdew, J. P.; Burke, K.; Ernzerhof, M., Generalized Gradient Approximation Made Simple. *Phys. Rev. Lett.* **1996,** *77*, 3865-3868.
37. Monkhorst, H. J.; Pack, J. D., Special Points for Brillouin-Zone Integrations. *Phys. Rev. B* **1976,** *13*, 5188-5192.
38. Yamamoto, N.; Endo, T.; Shimada, M.; Takada, T., Single Crystal Growth of α-MnO_2. *Jpn. J. Appl. Phys.* **1974,** *13*, 723-724.
39. Guo, H.; Zhang, Y.; Marschilok, A. C.; Takeuchi, K. J.; Takeuchi, E. S.; Liu, P., A First Principles Study of Spinel $ZnFe_2O_4$ for Electrode Materials in Lithium-Ion Batteries. *Phys. Chem. Chem. Phys.* **2017,** *19*, 26322-26329.
40. Zhang, Y.; Pelliccione, C. J.; Brady, A. B.; Guo, H.; Smith, P. F.; Liu, P.; Marschilok, A. C.; Takeuchi, K. J.; Takeuchi, E. S., Probing the Li Insertion Mechanism of $ZnFe_2O_4$ in Li-Ion Batteries: A Combined X-Ray Diffraction, Extended X-Ray Absorption Fine Structure, and Density Functional Theory Study. *Chem. Mater.* **2017,** *29*, 4282-4292.
41. Wang, L.; Zhang, Y.; Guo, H.; Li, J.; Stach, E. A.; Tong, X.; Takeuchi, E. S.; Takeuchi, K. J.; Liu, P.; Marschilok, A. C.; et al., Structural and Electrochemical Characteristics of Ca-Doped "Flower-like" $Li_4Ti_5O_{12}$ Motifs as High-Rate Anode Materials for Lithium-Ion Batteries. *Chem. Mater.* **2018,** *30*, 671-684.
42. Rossouw, M. H.; Liles, D. C.; Thackeray, M. M.; David, W. I. F.; Hull, S., Alpha Manganese Dioxide for Lithium Batteries: A Structural and Electrochemical Study. *Mater. Res. Bull.* **1992,** *27*, 221-230.
43. Van Vleck, J., The Jahn-Teller Effect and Crystalline Stark Splitting for Clusters of the Form XY6. *J. Chem. Phys.* **1939,** *7*, 72-84.
44. Cabana, J.; Monconduit, L.; Larcher, D.; Palacín, M. R., Beyond Intercalation-Based Li-Ion Batteries: The State of the Art and Challenges of Electrode Materials Reacting Through Conversion Reactions. *Adv. Mater.* **2010,** *22*, E170-E192.
45. Obrovac, M. N.; Christensen, L.; Le, D. B.; Dahn, J. R., Alloy Design for Lithium-Ion Battery Anodes. *J. Electrochem. Soc.* **2007,** *154*, A849-A855.
46. Kitchaev, D. A.; Dacek, S. T.; Sun, W.; Ceder, G., Thermodynamics of Phase Selection in MnO_2 Framework Structures through Alkali Intercalation and Hydration. *J. Am. Chem. Soc.* **2017,** *139*, 2672-2681.
47. Crespo, Y.; Seriani, N., Electronic and Magnetic Properties of α-MnO_2 from Ab Initio Calculations. *Phys. Rev. B* **2013,** *88*, 144428.
48. Duan, X.; Yang, J.; Gao, H.; Ma, J.; Jiao, L.; Zheng, W., Controllable Hydrothermal Synthesis of Manganese Dioxide Nanostructures: Shape Evolution, Growth Mechanism and Electrochemical Properties. *CrystEngComm* **2012,** *14*, 4196-4204.
49. Huang, X.; Lv, D.; Yue, H.; Attia, A.; Yang, Y., Controllable Synthesis of α-and β-MnO_2: Cationic Effect on Hydrothermal Crystallization. *Nanotechnology* **2008,** *19*, 225606.

50. Portehault, D.; Cassaignon, S.; Baudrin, E.; Jolivet, J.-P., Structural and Morphological Control of Manganese Oxide Nanoparticles upon Soft Aqueous Precipitation through MnO_4^-/Mn^{2+} Reaction. *J. Mater. Chem.* **2009,** *19*, 2407-2416.
51. Yin, B.; Zhang, S.; Jiang, H.; Qu, F.; Wu, X., Phase-Controlled Synthesis of Polymorphic MnO_2 Structures for Electrochemical Energy Storage. *J. Mater. Chem. A* **2015,** *3*, 5722-5729.
52. Tian, Z.-R.; Xia, G.; Luo, J.; Suib, S. L.; Navrotsky, A., Effects of Water, Cations, and Structure on Energetics of Layer and Framework Phases, $Na_xMg_yMnO_2 \cdot nH_2O$. *J. Phys. Chem. B* **2000,** *104*, 5035-5039.
53. Wu, H.-C.; Lin, S.-W.; Wu, J.-S., Effects of Nitrogen Concentration on N-Doped Anatase TiO_2: Density Functional Theory and Hubbard U Analysis. *J. Alloys Comp.* **2012,** *522*, 46-50.
54. Zhao, Z.; Liu, Q., Designed Highly Effective Photocatalyst of Anatase TiO_2 Codoped with Nitrogen and Vanadium Under Visible-light Irradiation Using First-principles. *Catal. Lett.* **2008,** *124*, 111-117.
55. Jain, A.; Hautier, G.; Moore, C. J.; Ping Ong, S.; Fischer, C. C.; Mueller, T.; Persson, K. A.; Ceder, G., A High-Throughput Infrastructure for Density Functional Theory Calculations. *Comp. Mater. Sci.* **2011,** *50*, 2295-2310.
56. Jain, A.; Ong, S. P.; Hautier, G.; Chen, W.; Richards, W. D.; Dacek, S.; Cholia, S.; Gunter, D.; Skinner, D.; Ceder, G.; et al., The Materials Project: A Materials Genome Approach to Accelerating Materials Innovation. *APL Mater.* **2013,** *1*, 011002.

TOC

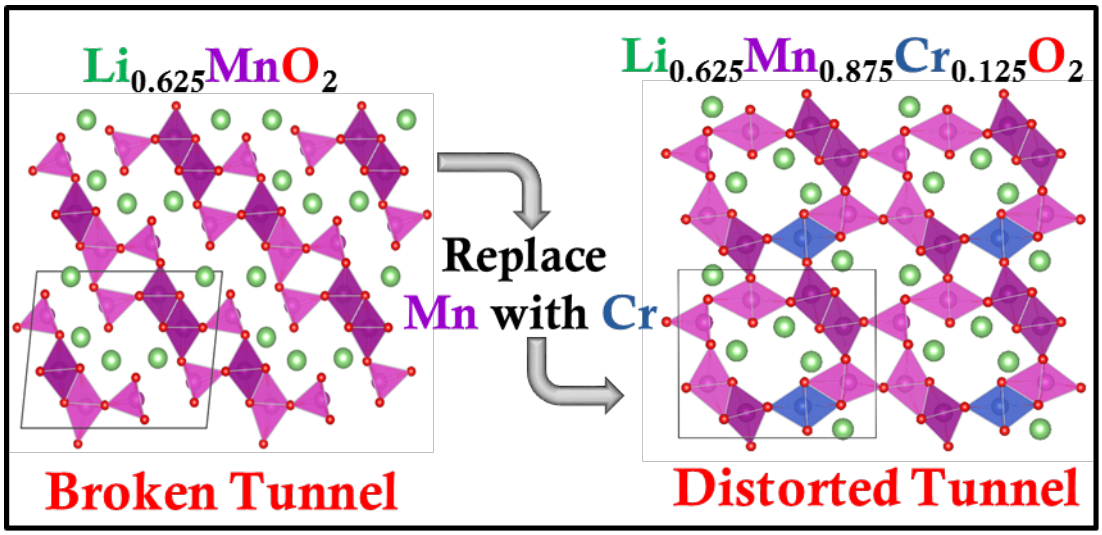
$Li_{0.625}MnO_2$
$Li_{0.625}Mn_{0.875}Cr_{0.125}O_2$
Replace
Mn with Cr
Broken Tunnel
Distorted Tunnel